Using Numerical Dissipation Rate and Viscosity to Assess Turbulence-Related Data Accuracy – Part 2: Results

Vojtěch Turek, Zdeněk Jegla*, Miloslav Dohnal, and Marcus Reppich*

DOI: 10.1002/cite.202200045

Supporting Information available online

This is the second part of a two-part paper focusing on the assessment of accuracy of turbulence-related data from CFD simulations using effective numerical dissipation rate and effective numerical viscosity. Experimental setup has been discussed in the first part of this series. Here, the relevant solution data obtained via CFD are compared to the values from laser Doppler anemometry measurements, and it is studied whether the accuracy of such data can be assessed using the two mentioned quantities. The overall outcome is that although judging mesh quality generally is possible, alone the two quantities are insufficient to draw conclusions regarding the actual solution data.

Keywords: Computational fluid dynamics, Numerical dissipation, Numerical viscosity, Reynolds stress tensor

Received: April 11, 2022; *revised:* June 22, 2022; *accepted:* August 30, 2022

1 Introduction

The first paper of this two-part series [1] discussed the experimental setup involving the flow system from Fig. 1. The present, second paper reports the actual results of the study, i.e., it lists the relevant solution data exported from the evaluated computational fluid dynamics (CFD) cases and compares them to the reference data from laser Doppler anemometry (LDA) measurements [2]. Due to the limited space available, however, selected data are presented as Supporting Information (SI).

Compared to the physical experiment presented in [2], which involved a swirl generator, in the CFD cases discussed further the pipe inlet velocity was directly specified using the corresponding velocity profile providing all three velocity components (axial, radial, and tangential). Moreover, because the present paper focused on engineering applications of CFD where a compromise between data accuracy and computational demand is always sought, the k–ω SST SAS (shear stress transport scale-adaptive simulation) [3] and WMLES (wall-modeled large eddy simulation) [4] turbulence models were employed.

The CFD cases were evaluated in ANSYS Fluent 2019 R3 [5], used five different-quality hexahedral and polyhedral meshes ranging from 0.950 million cells to 20.6 million cells, and included the computation of effective numerical dissipation rate and effective numerical viscosity at the individual cell level via the procedure proposed by Schranner et al. [6]. To keep computational times manageable, the WMLES-based cases featured a shorter pipe segment (1 m instead of 5 m, i.e., only up to $L/D = 17.3$). Refer to [1] for a detailed description of the meshes, CFD setup, etc.

The normalized mean velocity profiles on the individual interrogation line segments are discussed in Sect. 2. The plots of normalized mean distributions of the diagonal and off-diagonal components of the Reynolds stress tensor are shown in Sect. 3 and 4. Sect. 5. presents the mean effective numerical dissipation rates and mean effective numerical viscosity values yielded by the individual CFD simulations. Conclusions of this study are summarized in Sect. 6.

[1]Dr.-Ing. Vojtěch Turek, [1]Dr.-Ing. Zdeněk Jegla (Zdenek.Jegla@vut.cz), [2]Dipl.-Ing. Miloslav Dohnal, [1,3]Prof. Dr.-Ing. Marcus Reppich (marcus.reppich@hs-augsburg.de)

[1]Brno University of Technology, Faculty of Mechanical Engineering, Institute of Process Engineering, Technická 2, 61669 Brno, Czech Republic.

[2]SVS FEM s.r.o., Trnkova 3104, 62800 Brno, Czech Republic.

[3]Augsburg University of Applied Sciences, Faculty of Mechanical and Process Engineering, An der Hochschule 1, 86161 Augsburg, Germany.

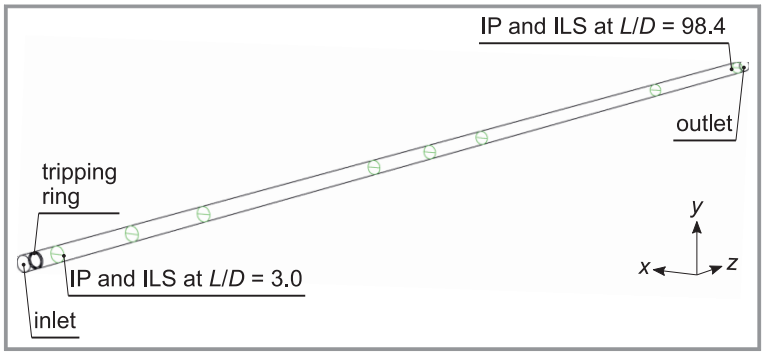

Figure 1. 3D visualization of the investigated flow system; IP and ILS denote interrogation plane and interrogation line segment, respectively. The measurement locations were at L/D = 3.0, 10.0, 17.3, 37.3, 44.8, 52.3, 81.7, and 98.4, where L denotes the downstream distance from the inlet and D the diameter of the pipe. (Reprinted from [1])

2 Normalized Mean Velocity Profiles

The first step in analyzing the solution data was concerned with the normalized mean velocity profiles. The corresponding axial (streamwise), radial, and tangential components obtained at the interrogation line segments were compared to the reference data from LDA measurements [2]. Better accuracy generally was observed in the turbulent core near the outlet of the modeled pipe segment where the flow had partly stabilized. The near-wall predictions of models employing the meshes without resolved boundary layers obviously were of much lower quality. Of interest was the fact the coarsest hexahedral mesh (0.950 million cells) performed better in terms of the mean axial velocity profiles than the slightly finer (1.35 million cells) one. The structure of this second mesh also seemed to be responsible for the observed dips and sharp corners in the profiles close to the pipe inlet. The polyhedral (1.94 million cells) mesh provided data of middling accuracy. As for the finest (20.6 million cells) hexahedral mesh, it did not seem to lead to any marked improvement compared to the second-finest (2.64 million cells) one in spite of the cell count being one order of magnitude larger.

More detailed information together with the plots of the normalized mean velocity profiles can be found in Sect. S1 of the SI. Also provided are the plots of absolute errors with respect to the reference data. Relative error plots were not generated because of the issues arising from the reference values often being near or crossing the zero line.

3 Normalized Mean Distributions of the Diagonal Components of the Reynolds Stress Tensor

Figs. 2–6 show the mean distributions of the diagonal components of the Reynolds stress tensor, τ''_{ii}, normalized using the overall mean flow velocity, $u_m = 2.34\,m\,s^{-1}$ (this corresponds to the total mass flow rate of $3.8135\,kg\,s^{-1}$; see [1]). In the plots, R denotes the radius of the pipe, $r/R \in [-1, 1]$ the normalized coordinate along the respective interrogation line segment, L the downstream distance from the swirl generator, and D the diameter of the pipe. Subscripts "a", "r", and "t" denote the axial (streamwise), radial, and tangential components, and "(ref.)" the reference values from the paper by Pashtrapanska et al. [2].

The first set of plots (Fig. 2) pertains to the first CFD case, which utilized the k–ω SST SAS turbulence model and the coarsest hexahedral mesh (0.950 million cells). One can see

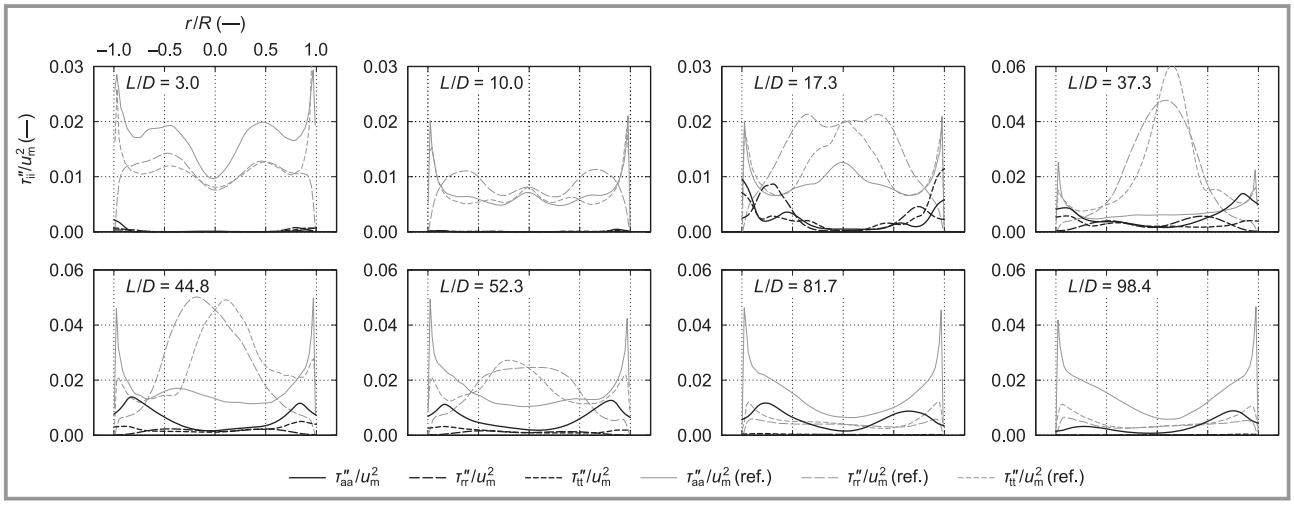

Figure 2. Normalized mean distributions of the diagonal components of the Reynolds stress tensor on the respective interrogation line segments exported from the first CFD case (hexahedral mesh, 0.950 million cells, k–ω SST SAS turbulence model).

that at L/D = 3.0 and 10.0, the predicted values were close to zero across the entire interrogation line segments, i.e., they were very different from the reference data. Only from L/D = 37.3 the axial-axial profile started to resemble the reference one, but the discrepancy was large, nonetheless. The other two predicted profiles (radial-radial and tangential-tangential) did not resemble the reference data at all.

The predicted normalized mean distributions of the diagonal components of the Reynolds stress tensor obtained using the slightly finer hexahedral mesh (1.35 million cells) are shown in Fig. 3. Just as before, all three distributions were near zero at L/D = 3.0 and L/D = 10.0. At higher L/D, the predicted distributions generally were asymmetrical even though the reference data featured relative symmetry around r/R = 0. The best fit (trend-wise) could be observed at L/D = 37.3; however, even there the absolute errors in the radial-radial and tangential-tangential distributions remained large. It was apparent that the CFD model, which made use of the Boussinesq eddy viscosity approximation, was not able to match the observed turbulence anisotropy at all even when the respective finer structured hexahedral mesh was employed.

When the polyhedral mesh consisting of 1.94 million cells was used, the predicted distributions resembled the reference data much better (see Fig. 4). In this case, values significantly greater than zero were obtained except for the radial-radial and tangential-tangential distributions at $L/D \geq 81.7$. The axial-axial distribution again featured the best fit, but some similarity could also be observed in the other two distributions at $L/D \leq 17.3$. As for the near-wall region, the predictions were of higher quality than before, yet significant discrepancies were still present. This was most likely due to the better predictive capability of k–ω SST SAS on polyhedral meshes [7].

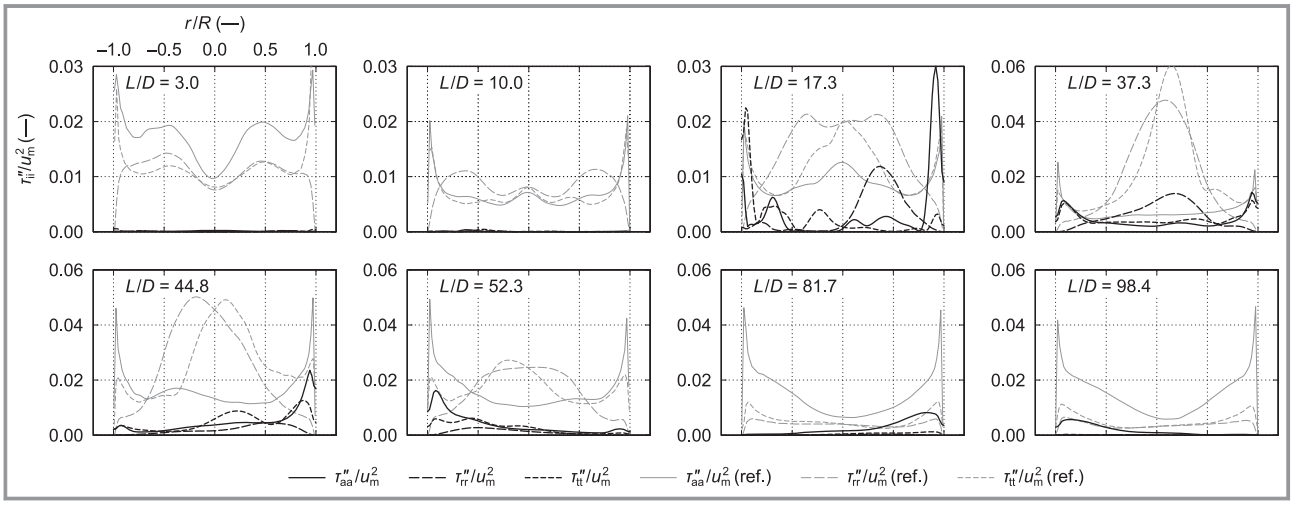

Figure 3. Normalized mean distributions of the diagonal components of the Reynolds stress tensor on the respective interrogation line segments exported from the second CFD case (hexahedral mesh, 1.35 million cells, k–ω SST SAS turbulence model).

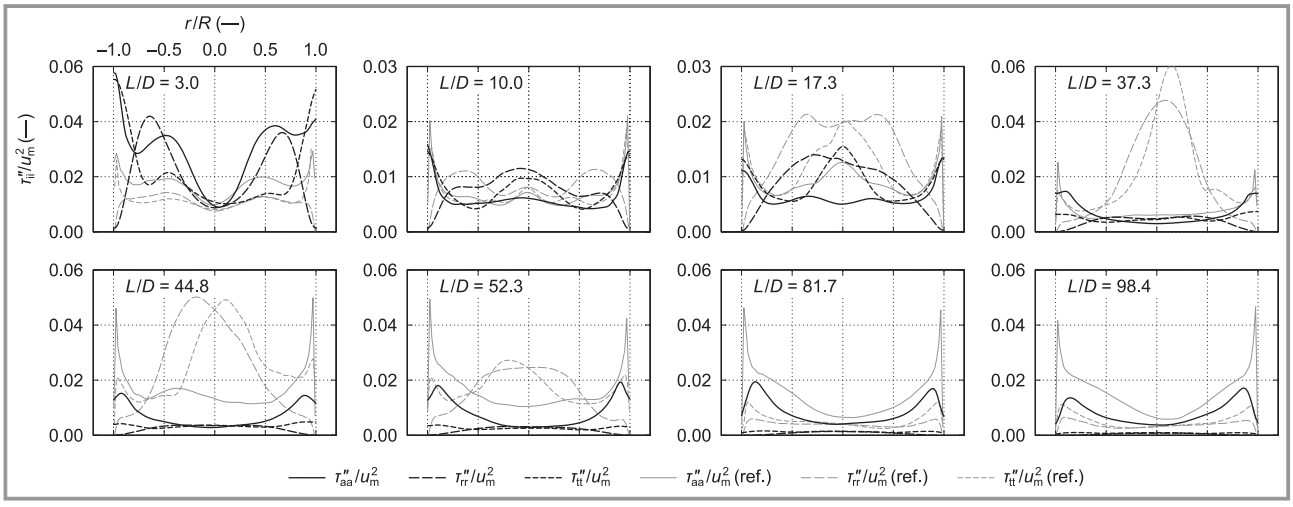

Figure 4. Normalized mean distributions of the diagonal components of the Reynolds stress tensor on the respective interrogation line segments exported from the third CFD case (polyhedral mesh, 1.94 million cells, k–ω SST SAS turbulence model).

The normalized mean distributions of the diagonal components of the Reynolds stress tensor yielded by the first CFD case utilizing the WMLES turbulence model can be found in Fig. 5. Here, the hexahedral mesh consisted of 2.64 million cells. Even though the discrepancies were non-negligible, at least trend-wise the distributions mostly conformed to the reference data. What was more, one could also see marked improvement in accuracy near the pipe wall due to the region being resolved much better.

The normalized mean distributions of the diagonal components of the Reynolds stress tensor obtained using the finest hexahedral mesh (20.6 million cells) and the WMLES turbulence model (see Fig. 6) were very similar to those obtained using the much smaller mesh and the otherwise identical CFD setup. Although some trends featured slightly better accuracy, it was obvious that such a large mesh was far beyond the point of diminishing returns. See Sect. S2 for the respective absolute error plots.

4 Normalized Mean Distributions of the Off-Diagonal Components of the Reynolds Stress Tensor

Analogously to the previous set of plots, the following set (Figs. 7–11) provides the normalized mean distributions of the off-diagonal components of the Reynolds stress tensor, τ''_{ij}. From the results in Fig. 7, which were obtained using the coarsest hexahedral mesh (0.950 million cells), it can be seen that at L/D = 3.0 and L/D = 10.0 the predicted values were close to zero across the entire interrogation line segments. A hint of similarity could only be observed between the predicted and reference axial-radial and axial-tangential distributions at L/D = 81.7. Considering the radial-tangential distributions at $L/D \geq 37.3$, these were missing in the reference data set [2] and, therefore, could not be compared.

With the hexahedral mesh consisting of 1.35 million cells, the results, too, were very different from the reference data (see Fig. 8). Moreover, the predicted off-diagonal components of the Reynolds stress tensor at L/D = 3.0 and 10.0 were again close to zero.

When the polyhedral mesh (1.94 million cells) was used, the predicted normalized off-diagonal components of the Reynolds stress tensor were as shown in Fig. 9. Although the obtained trends generally were different from the reference ones, some similarity could be seen in the axial-radial component at $L/D \geq 81.7$, axial-tangential component at L/D = 81.7, and radial-tangential component at $L/D \leq 17.3$ (reference radial-tangential data for further locations were not available in [2]).

Fig. 10 shows the normalized data yielded by the WMLES-based model utilizing the coarser mesh (2.64 million cells). At L/D = 3.0, none of the three trends

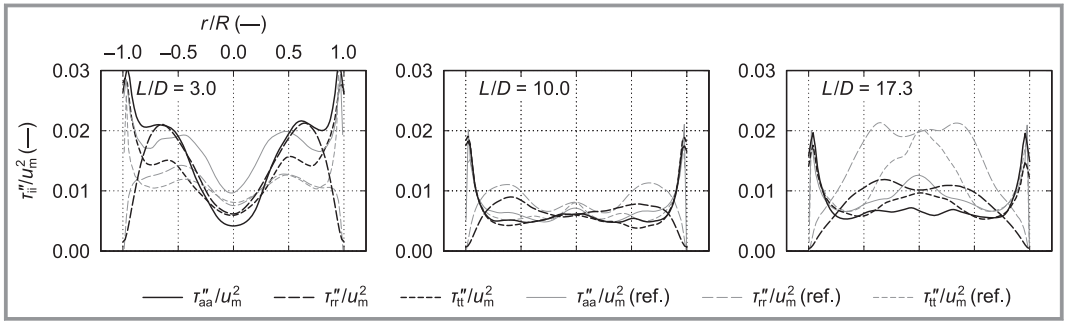

Figure 5. Normalized mean distributions of the diagonal components of the Reynolds stress tensor on the respective interrogation line segments exported from the fourth CFD case (hexahedral mesh, 2.64 million cells, WMLES turbulence model).

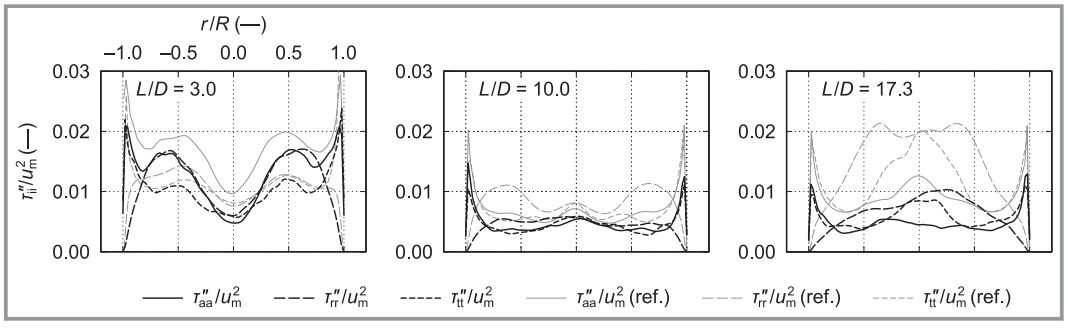

Figure 6. Normalized mean distributions of the diagonal components of the Reynolds stress tensor on the respective interrogation line segments exported from the fifth CFD case (hexahedral mesh, 20.6 million cells, WMLES turbulence model).

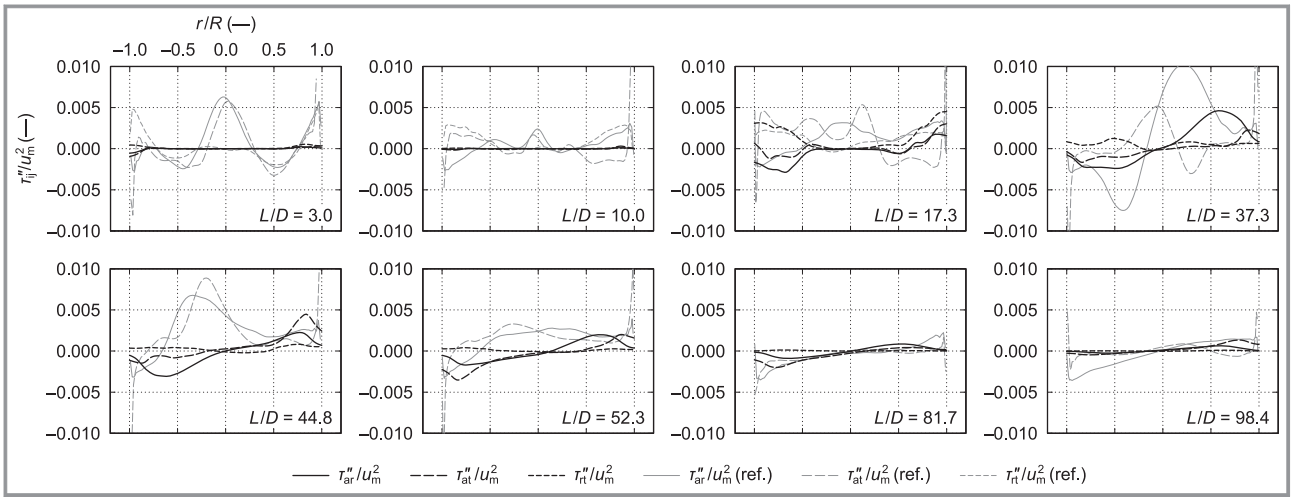

Figure 7. Normalized mean distributions of the off-diagonal components of the Reynolds stress tensor on the respective interrogation line segments exported from the first CFD case (hexahedral mesh, 0.950 million cells, *k*–*ω* SST SAS turbulence model). Please note that there were no reference data in [2] for normalized τ''_{rt} at $L/D \geq 37.3$.

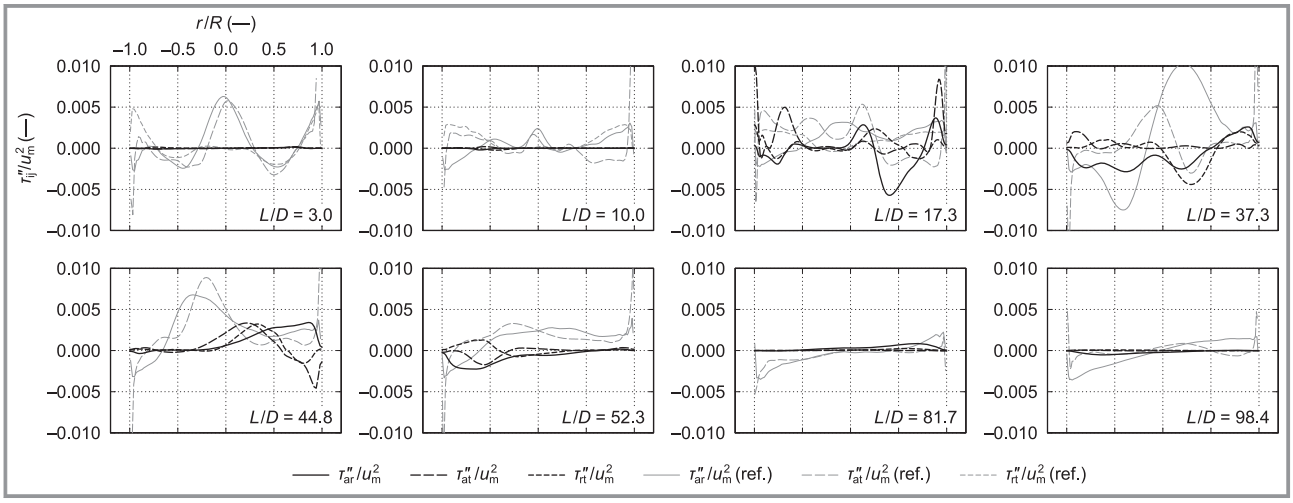

Figure 8. Normalized mean distributions of the off-diagonal components of the Reynolds stress tensor on the respective interrogation line segments exported from the second CFD case (hexahedral mesh, 1.35 million cells, *k*–*ω* SST SAS turbulence model). Please note that there were no reference data in [2] for normalized τ''_{rt} at $L/D \geq 37.3$.

corresponded to the reference data. If the small peaks around $r/R = 0.0$ were disregarded in the plot for $L/D = 10.0$, then there the predicted data were relatively close to the reference values. At $L/D = 17.3$, the radial-tangential component matched the reference data quite well while the remaining two components featured larger discrepancies. This most likely was a consequence of the turbulence anisotropy observed in the reference data, which started to increase at around $L/D = 17.3$ (see Sect. 3) in combination with the CFD model employing the Boussinesq approximation.

In the last CFD case utilizing the finest mesh (20.6 million cells) and the WMLES turbulence model, the results (shown in Fig. 11) were akin to those from Fig. 10. In other words, one could observe no similarity between the predicted and reference trends at $L/D = 3.0$, at $L/D = 10.0$ all trends matched reasonably well except for the small central peaks, and at $L/D = 17.3$ only the radial-tangential data were relatively close to the reference values. Again, it was clear that using such a large mesh brought no advantage whatsoever. The corresponding absolute error plots are provided in the SI in Sect. S3.

5 Mean Effective Numerical Dissipation Rate and Mean Effective Numerical Viscosity

Mean effective numerical dissipation rate, ε_n, and mean effective numerical viscosity, ν_n, data obtained using the procedure proposed by Schranner et al. [6] were exported

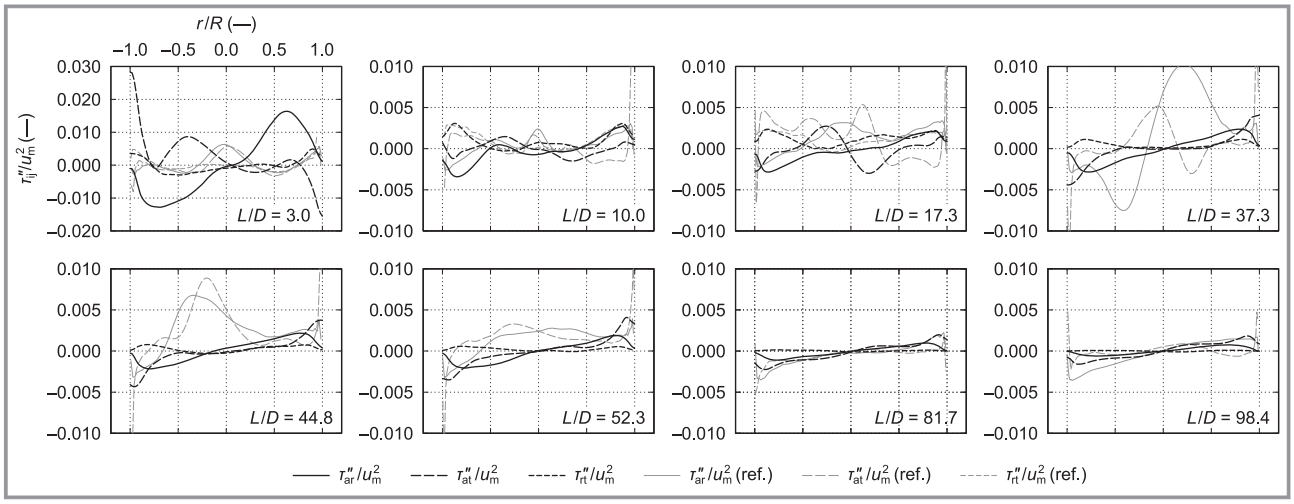

Figure 9. Normalized mean distributions of the off-diagonal components of the Reynolds stress tensor on the respective interrogation line segments exported from the third CFD case (polyhedral mesh, 1.94 million cells, k–ω SST SAS turbulence model). Please note that there were no reference data in [2] for normalized τ_{rt}'' at $L/D \geq 37.3$.

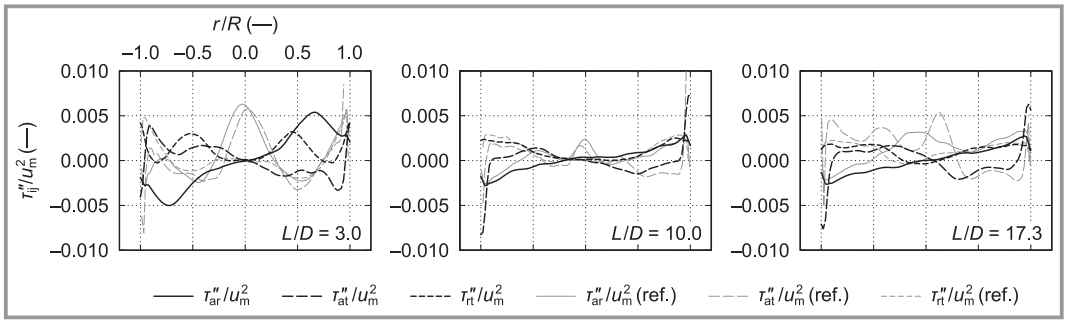

Figure 10. Normalized mean distributions of the off-diagonal components of the Reynolds stress tensor on the respective interrogation line segments exported from the fourth CFD case (hexahedral mesh, 2.64 million cells, WMLES turbulence model).

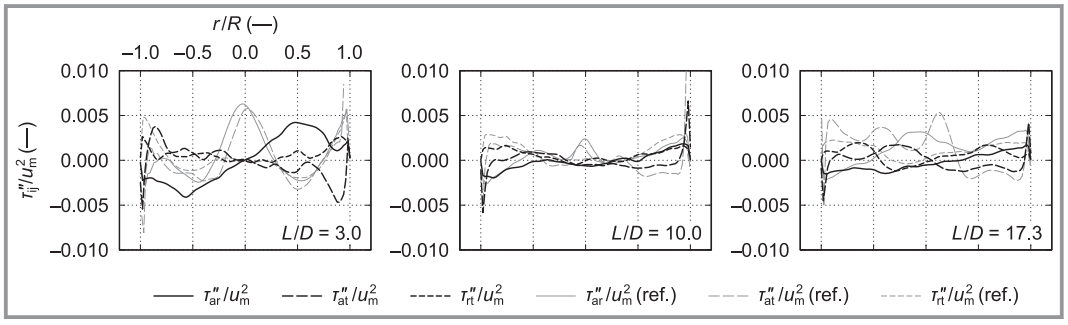

Figure 11. Normalized mean distributions of the off-diagonal components of the Reynolds stress tensor on the respective interrogation line segments exported from the fifth CFD case (hexahedral mesh, 20.6 million cells, WMLES turbulence model).

from the CFD cases for the entire interrogation planes (see Fig. 1) instead of the interrogation line segments used previously. When $\varepsilon_n > 0$, the rate of dissipation of kinetic energy was greater than expected given the changes in the other quantities. Otherwise, when $\varepsilon_n < 0$, the rate of dissipation was smaller than expected. Effective numerical viscosity, on the other hand, represented a measure of change in effective viscosity of the fluid caused by discretization. Please note that the effective numerical viscosity, as defined in [6], was not a direct equivalent to the physical viscosity.

The observed values of mean effective numerical dissipation rate decreased in absolute size towards the pipe outlet, but with all hexahedral meshes except the finest one their underlying cell structures could easily be seen in the plots

for $L/D \leq 17.3$. The plots corresponding to the polyhedral mesh did not feature any distinct pattern. As for mean effective numerical viscosity, largest values (in absolute size) were reported in the core of the flow and generally increased from the pipe inlet towards its other end. In the near-wall regions, the discussed quantity remained close to zero. Although the underlying cell structure was only apparent in the plots obtained using the 2.64 million cell hexahedral mesh, in all five CFD cases there were multiple cell regions where negative numerical viscosity was reported, which could have had adverse effect on the stability of the employed numerical schemes. Overall, from the data it was obvious that the hexahedral meshes were not suitable due to poor cell alignment with the flow. Please refer to Sect. S4 for the contour plots in question as well as a brief discussion regarding the data.

It is obvious that the solution data presented in Sects. 2–4 and as part of the Supporting Information were influenced by the cumulative effect of the discretization-induced numerical errors all the way from the pipe inlet to the actual interrogation line segments. Therefore, it made more sense to consider as decision parameters the aggregate values of mean effective numerical dissipation rate and mean effective numerical viscosity per the entire computational domain. These are listed in Tab. 1, in which an overall mean value corresponds to the sum over the entire computational domain of the time-averaged cell values. A cell mean value, on the other hand, is a time and volume-weighted average value per one cell. The obtained cell mean values were most important because they did not depend on the total number of cells or the physical size of the computational domain.

With respect to how effective numerical dissipation rate and effective numerical viscosity were defined in the paper by Schranner et al. [6], lower absolute values of both these metrics should indicate lower induced numerical errors (i.e., higher-quality mesh). This correlated with the decreasing absolute errors in the observed quantities presented earlier when moving between the hexahedral meshes (cases 1, 2, 4, and 5). However, it also is apparent from Tab. 1 that the lowest values of the two discussed metrics were obtained using the polyhedral mesh consisting of just 1.94 million cells (case 3), yet there the solution data accuracy generally was lower than when the finer hexahedral meshes were employed. This provided the answer to the research hypothesis ("Can ε_n and ν_n be used to assess the accuracy of the obtained turbulence-related data?") without having to evaluate further CFD cases involving, e.g., tetrahedral meshes. It also meant that the utilized cell type had significant influence on the values of the two metrics even when the respective mesh cell counts were similar.

6 Conclusions

Five different CFD cases with meshes ranging from 0.950 million cells to 20.6 million cells were evaluated to determine whether effective numerical dissipation rate, ε_n, and effective numerical viscosity, ν_n, could be used to assess the accuracy of the obtained turbulence-related data. Both structured and unstructured hexahedral and polyhedral meshes were considered to establish whether the cell type significantly influenced the obtained values of ε_n and ν_n. Two turbulence models most commonly used in process and power engineering simulations, namely k–ω SST SAS and WMLES, were utilized in the evaluated CFD cases.

The first step in the analysis of solution data from the CFD simulations comprised the comparison of normalized mean axial, radial, and tangential velocity profiles to the LDA data from literature. Here, it was found that the agreement between the velocity profiles was gradually improving from the instability-generating tripping ring towards the outlet of the modeled pipe segment, that is, the models were able to better predict the flow only once the fluid motion had partly stabilized. The axial profiles generally were predicted with better accuracy than the radial and tangential ones. It also was of note that although the axial profiles from LDA were relatively symmetrical along the entire pipe segment, the profiles predicted using the coarser hexahedral meshes featured at multiple locations non-negligible asymmetry.

The primary focus of this study was the prediction of normalized mean distributions of the Reynolds stress tensor components in relation to the two metrics (ε_n and ν_n) mentioned above. Data obtained using the two coarsest hexahedral meshes – of which the finer one contained a boundary cell layer – generally were very different from the reference values from LDA measurements. The diagonal profiles also were largely asymmetrical despite the reference data featuring relative symmetry. In the two corresponding

Table 1. Overall mean (time-averaged cell values summed over the entire computational domain) and cell mean (time and volume-weighted average per cell) effective numerical dissipation rates (ε_n) and effective numerical viscosities (ν_n).

Case No.	Overall mean ε_n [kg m^{2}s^{-3}]	Cell mean ε_n [kg m^{2}s^{-3}]	Overall mean ν_n [m^{2}s^{-1}]	Cell mean ν_n [m^{2}s^{-1}]
1	$-1.384 \cdot 10^5$	$-1.483 \cdot 10^{-1}$	$-1.426 \cdot 10^7$	$-1.252 \cdot 10^1$
2	$-1.462 \cdot 10^5$	$-1.198 \cdot 10^{-1}$	$-1.419 \cdot 10^7$	$-1.126 \cdot 10^1$
3	$1.222 \cdot 10^3$	$5.736 \cdot 10^{-4}$	$3.214 \cdot 10^5$	$1.670 \cdot 10^{-1}$
4	$16.013 \cdot 10^3$	$6.621 \cdot 10^{-3}$	$13.862 \cdot 10^5$	$5.081 \cdot 10^{-1}$
5	$-16.122 \cdot 10^3$	$-9.625 \cdot 10^{-4}$	$-5.909 \cdot 10^6$	$-3.380 \cdot 10^{-1}$

CFD cases, the cell mean effective numerical dissipation rates were of the order of $10^{-1}\,kg\,m^2s^{-3}$ and the cell mean effective numerical viscosities of the order of $10^{1}\,m^2s^{-1}$ (with the values being smaller in absolute size when the finer mesh was employed). On the other end of the fineness spectrum were the remaining two hexahedral meshes. With these, prediction accuracy improved significantly, but many profiles still matched the reference data only trend-wise (if at all). As for the two metrics, here the cell mean effective numerical dissipation rates were of the order of $10^{-3}\,kg\,m^2s^{-3}$ and $10^{-4}\,kg\,m^2s^{-3}$ (values smaller in absolute size were obtained using the very fine, 20.6 million cell mesh) and the cell mean effective numerical viscosities of the order of $10^{-1}\,m^2s^{-1}$ (in both cases). In other words, the gradual improvements in solution data accuracy across the four hexahedral meshes correlated with the decreasing absolute sizes of the two monitored metrics. However, with the relatively coarse polyhedral mesh, which led to solution data of middling accuracy, the cell mean effective numerical dissipation rate and cell mean effective numerical viscosity were the lowest overall (in absolute size), although still of the orders identical to the ones observed with the most detailed, 20.6 million cell mesh. The respective variability effectively led to omitting the evaluation of tetrahedral meshes, because the answer to the research hypothesis was clear without the need for any such CFD cases.

The contour plots of mean effective numerical dissipation rate and mean effective numerical viscosity revealed that the hexahedral meshes could not cope with the swirling nature of the flow as well as the polyhedral mesh due to problematic alignment of the cells with the flow. Moreover, the mean effective numerical viscosity being in some cell regions negative and large in absolute size suggested that there the stability of the employed numerical schemes may have been decreased. Also of interest was the fact that meshes of similar sizes (in terms of cell count) but with different topologies led to markedly different results.

The only explanation for the variation in the presented metrics with respect to solution data accuracy was that the hexahedral meshes were unsuitable due to problematic alignment with the modeled swirling pipe flow. Cells in the polyhedral mesh, on the other hand, were much more similar to the ideal cell (a sphere), and, consequently, the induced numerical errors were lower even if the total number of cells in the domain was one order of magnitude lower (1.94 million vs. 20.6 million). In other words, although some accuracy was gained in cases 4 & 5 by better resolving the near-wall region etc., some of it also was lost (compared to case 3) because of poor cell alignment with the flow. Moreover, this effect was compounded in case 3 by utilizing the k–ω SST SAS turbulence model known to perform very well on polyhedral meshes.

The overall conclusion, therefore, is that the two metrics proposed by Schranner et al. [6] can be used to assess mesh quality but alone are not sufficient when it comes to assessing the quality of the obtained solution data.

It is important to note that the employed CFD models were based on the Boussinesq approach, which assumes the turbulent viscosity to be an isotropic scalar quantity. Although this simplification is very often used in engineering applications of CFD, making use of the Reynolds Stress Model (RSM) [8], which solves transport equations for each component of the Reynolds stress tensor, would obviously lead to better-quality data. Therefore, RSM is one of the possible future research avenues considering the turbulence anisotropy commonly observed in swirling pipe flows. Similarly, given the asymmetry of the data from CFD simulations presented in this paper, it would be interesting to compare the performance of the models if both temporal and spatial (over concentric rings of suitable widths) averaging were employed. This, however, would require a reference data set different from the one used here.

Another possible future research direction is finding other metrics which, when considered together with effective numerical dissipation rate and effective numerical viscosity, could be used for the mentioned purpose.

Supporting Information

Supporting Information for this article can be found under DOI: https://doi.org/10.1002/cite.202200045.

Acknowledgment

This research was funded by the Czech Ministry of Education, Youth, and Sports/EU Operational Programme Research, Development and Education, grant No. CZ.02.1.01/0.0/0.0/16_026/0008413 “Strategic partnership for environmental technologies and energy production”. Open access funding enabled and organized by Projekt DEAL.

Symbols used

D	[m]	diameter of the pipe
k	[m^2s^{-2}]	turbulence kinetic energy
L	[m]	downstream distance from the swirl generator
R	[m]	radius of the pipe
r	[m]	radial location on an interrogation line segment, m
$\bar{u}$	[$m\,s^{-1}$]	mean flow velocity
u_m	[$m\,s^{-1}$]	overall mean flow velocity
x, y, z	[–]	directions in the coordinate system

Greek letters

ε_n	[$kg\,m^2s^{-3}$]	effective numerical dissipation rate
ν_n	[m^2s^{-1}]	effective numerical viscosity

τ''	$[m^2s^{-2}]$	component of the Reynolds stress tensor
ω	$[s^{-1}]$	turbulence eddy frequency

Sub- and Superscripts

a	axial component
CFD	value obtained using a CFD model
i, j	indices of components
r	radial component
ref.	reference value
t	tangential component

Abbreviations

CFD	Computational Fluid Dynamics
ILS	interrogation line segment
IP	interrogation plane
LDA	Laser Doppler Anemometry
RSM	Reynolds Stress Model
SAS	Scale-Adaptive Simulation
SST	Shear Stress Transport
WMLES	Wall-Modeled Large Eddy Simulation

References

[1] V. Turek, Z. Jegla, M. Dohnal, M. Reppich, *Chem. Ing. Tech.* **2023**, in press. DOI: https://doi.org/10.1002/cite.202200044
[2] M. Pashtrapanska, J. Jovanović, H. Lienhart, F. Durst, *Exp. Fluids* **2006**, *41 (5)*, 813–827. DOI: https://doi.org/10.1007/s00348-006-0206-x
[3] F. R. Menter, Y. Egorov, *Flow Turbul. Combust.* **2010**, *85 (1)*, 113–138. DOI: https://doi.org/10.1007/s10494-010-9264-5
[4] M. L. Shur, P. R. Spalart, M. K. Strelets, A. K. Travin, *Int. J. Heat Fluid Flow* **2008**, *29 (6)*, 1638–1649. DOI: https://doi.org/10.1016/j.ijheatfluidflow.2008.07.001
[5] *ANSYS Fluent User's Guide, Version 2019 R3*, ANSYS, Inc., Canonsburgh, PA **2019**.
[6] F. S. Schranner, J. A. Domaradzki, S. Hickel, N. A. Adams, *Comput. Fluids* **2015**, *114*, 84–97. DOI: https://doi.org/10.1016/j.compfluid.2015.02.011
[7] Y. M. Shim, R. Sharma, P. Richards, in *Proc. of the 39th AIAA Fluid Dyn. Conf.*, American Institute of Aeronautics and Astronautics (AIAA), Reston, VA **2009**, AIAA 2009-4160.
[8] B. E. Launder, G. J. Reece, W. Rodi, *J. Fluid Mech.* **1975**, *68 (3)*, 537–566. DOI: https://doi.org/10.1017/S0022112075001814

